Distinct S wave reflector in the midcrust beneath Nikko-Shirane volcano in the northeastern Japan arc

Satoshi Matsumoto and Akira Hasegawa

Observation Center for Prediction of Earthquakes and Volcanic Eruptions, Faculty of Science, Tohoku University, Sendai, Japan

Abstract. Distinct S waves reflected from a midcrustal seismic velocity discontinuity are detected beneath Nikko-Shirane volcano in the southernmost part of the northeastern Japan arc. A detailed travel time analysis of the reflected S waves by using data acquired through a dense seismic network temporarily set up in this region shows that this unusual S wave reflector is distributed over an area of 15×15 km^2 at depths ranging from 8 to 15 km. The reflector has a conical shape becoming shallow toward the summit of Nikko-Shirane volcano. Observed amplitude spectral ratios of reflected S waves to direct S waves show that the reflector body has a strong velocity contrast to the surrounding medium and its thickness is of the order of 100 m at most. The reflector body is approximated by two thin layers probably filled with partially molten materials. Cutoff depth for shallow seismicity in this area is 3-5 km above the reflector and becomes shallow toward Nikko-Shirane volcano, nearly parallel to the reflector. The depth to brittle-ductile transition zone seems to be prescribed by the existence of the reflector body, which is perhaps a thin magma body.

Introduction

Nikko-Shirane volcano is located at the southernmost portion of the northeastern Japan arc, which is one of the most typical subduction zones in the world. many active volcanoes are distributed in this arc mainly along the volcanic front, which runs through the middle of the land area nearly parallel to the trench axis. Nikko-Shirane volcano, whose recent eruptions occurred in 1872, 1873, 1889, and 1952, is also right on the volcanic front. Seismic observations previously carried out around Nikko-Shirane volcano suggest the presence of a magma body in the midcrust beneath the volcano [*Mizoue*, 1980; *Mizoue et al.*, 1982; *Horiuchi et al.*, 1988].

Seismograms from shallow microearthquakes occurring to the south of the volcano contain a distinct S wave reflected phase (SxS) and an S-to-P mode-converted and reflected phase (SxP) from a midcrustal seismic velocity discontinuity. Observed amplitude ratios of SxP to SxS phases suggest the presence of a zone with a very low rigidity beneath the discontinuity [*Mizoue*, 1980]. *Mizoue et al.* [1982], based on data acquired through a temporary microearthquake observation network composed of four stations, located the depth of the discontinuity (S wave reflector) by using travel times of the SxS wave. Their result showed that the reflector has a depth of about 14 km beneath Ashio, about 15 km south-southeast of the volcano, and that it dips southeastward with an angle of 30-35 °.

In their analysis of locating the reflector, *Mizoue et al.* [1982] assumed that the top surface of the reflector is formed by a single horizontal plane, though the estimated one has a large dip angle of 30-35°. *Horiuchi et al.* [1988] carried out a temporary microearthquake observation with six telemetered stations in this area, and they mapped the depth distribution of the reflector by using both the SxS and SxP wave travel times.

Their assumption for locating the reflector was that the top surface of the reflector is a single plane with an arbitrary dip angle. The S wave reflector estimated from SxS wave travel times has the same location and configuration as that estimated from SxP waves, and it is distributed over an area of 10 km $\times$ 6 km southeast of Nikko-Shirane volcano at depths ranging 9-16 km. It dips southeastward with an angle of about 45°, becoming shallow toward the volcano.

A distinct S wave reflector, identical with that beneath Nikko-Shirane volcano, was first detected in the midcrust beneath the central Rio Grande Rift near Socorro, New Mexico [*Sanford et al.*, 1973]. Studies of *Sanford et al.* [1977] and *Rinehart et al.* [1979] indicate that a thin, relatively flat magma body at a depth of about 19 km is responsible for this anomalous reflector. *Ake and Sanford* [1988] used digitally recorded waveform data of the reflected phase to study the thickness and the nature of the magma body. By modeling the observed spectra of the reflected phase, they inferred that the magma body consists of a two-layered structure where a thin [about 70 m] layer of non rigid, low-velocity material overlies a second, thin [about 60 m] layer of slightly higher velocity material, the total thickness of the magma body being less than 150 m.

Anomalous S wave reflectors in the midcrust, similar to the Socorro magma body, have been detected so far at seven locations, including the Nikko-Shirane reflector, beneath the Japanese Islands [*Mizoue and Ishiketa*, 1988; *Iwase et al.*, 1989; *Nishiwaki et al.*, 1989; *Hori and Hasegawa*, 1991; *Inamori et al.*, 1992; *Hasegawa et al.*, 1991]. Five of them are found in the northeastern Japan arc. Tomographic inversions for P wave velocity recently made in this volcanic arc clearly delineate low-velocity zones continuously distributed from the upper crust right under active volcanoes to a depth of 100-150 km in the mantle wedge [*Hasegawa et al.*, 1991; *Zhao et al.*, 1992]. They are inclined to the west and are approximately parallel to the dip [$\sim$30°] of the underlying subducted Pacific plate. These low-velocity zones probably reflect the pathway of magma ascent
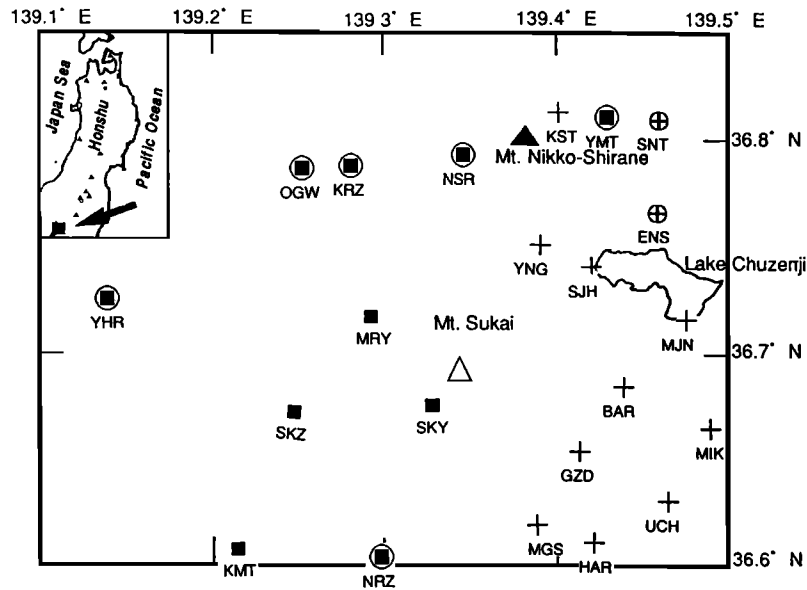
Figure 1. Map showing locations of seismic stations. Crosses and solid squares show stations set up in the 1989 and 1990 observations, respectively. Station symbols with open circles denote the stations at which SxS phases were not detected. Solid triangle denotes the location of an active volcano, Mount Nikko-Shirane.

from a deeper part of the mantle to the Earth's surface [*Hasegawa and Zhao*, 1994]. All of the midcrustal S wave reflectors detected at the five locations in this arc are located near active volcanoes and/or in or around the P wave low-velocity zones [*Hasegawa et al.*, 1991].

These seismic observations suggest a close relation of the distinct S wave reflector to the deep structure of arc volcanoes. In the present work, we try to investigate the geometry and the feature of the midcrustal S wave reflector beneath Nikko-Shirane volcano in more detail based on data acquired through temporary seismic observations with a dense station network.

Observations

In order to study the geometry and the nature of the distinct S wave reflector beneath Nikko-Shirane volcano, we carried out temporary observations with a dense seismic network in 1989 and in 1990. Locations of seismic stations are shown in Figure 1. Crosses and solid squares denote seismic stations set up in the 1989 and 1990 observations, respectively. Observation stations in the 1989 and 1990 observations are listed also in Table 1. Short-period seismometers with a natural frequency of 1 or 2 Hz were set up at the stations. Two- or three-component seismometers were installed at most of the stations. Seismic signals at each station were transmitted either with telephone telemetry or radio telemetry to a central station, passed through

an analog-to digital (AD) converter, and then recorded by using a personal computer at a sampling frequency of 200 Hz.

Seismicity in this area is quite high, and more than 10 microearthquakes per day are located by the present temporary observation network. Hypocenters located by the network are shown by open circles in Figure 2 [*Ito et al.*, 1994]. In the hypocenter determination, P and S wave velocities are assumed to be 6.0 km/s and 3.4 km/s, respectively. To avoid a systematic error in hypocenter locations arising from different combinations of stations, average values of travel time residuals both for P and S waves at each station are calculated and are used as station corrections in the hypocenter determination.

Most of microearthquakes in this area are distributed in two locations, as can be seen from Figure 2. One (Mt. Sukai group) is located near Mt. Sukai, and earthquakes are densely concentrated in this location at an average depth of about 5 km. The other (Ashio group) is around Ashio about 10 km southeast of the Mt. Sukai group. Earthquakes in this group are spatially much more sparse with an average focal depth of about 8 km. Hypocenter distribution is elongated from southwest to northeast. Seismic activity in this group was lower than that in the Mt. Sukai group for the investigated observation period. Typical fault plane solutions for the Ashio group, Mt. Sukai group and earthquakes that occurred beneath Mt. Nikko-Shirane are shown in Figure 2 [*Ito et al.*, 1994, 1995]. Reverse fault-type events having compression axes in the northwest-

Table 1. List of Stations in 1989 and 1990 Observations

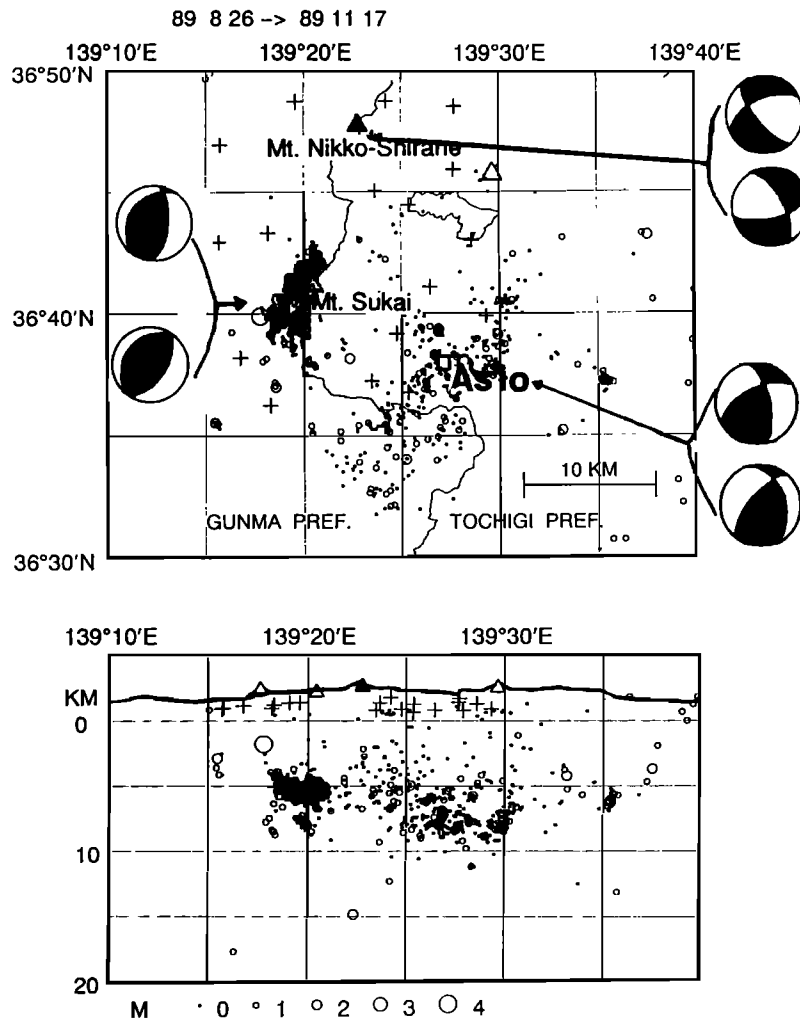|	Observation Period	Stations	Number of Earthquakes Located
1989	Aug.26 to Nov.17	BAR,MIK,GZD,MGS,UCH,HAR	1865
	Sep.12 to Oct.22	KST,SNT,YNG,ENS,SJH,MJN	
1990	Jun.29 to Aug.21	MGS,MIK,YMT,NSR,SRZ,OGW, MRY,SKY,SKZ,YHR,KMT,NRI	698

Figure 2. Hypocenter distribution of earthquakes in the Nikko-Ashio area determined by *Ito et al.* [1994] using temporary observation network data. Open circles and crosses denote locations of hypocenters and stations, respectively. The upper and lower figures show an epicenter distribution and an EW vertical cross-section of earthquakes, respectively. Solid line indicates surface topography.

southeast direction dominate in this region. This tendency is consistent with the regional stress field in and around the Nikko area [*Mochizuki et al.*, 1985]. On the contrary, earthquakes beneath Mt. Nikko-Shirane are not the reverse-fault type, but are characterized by normal faults. This suggests that the stress field beneath the summit of this volcano is locally in a tensional field. Recently, earthquakes similar to volcanic tremors have been detected at shallower depths (<2 km) just beneath the summit. Waveforms of these tremorlike earthquakes dominate low-frequency components with long duration times [*Ito et al.*, 1995].

An example of three-component seismograms for an event in the Ashio group is shown in Figure 3. We can see two distinct later phases in the seismogram. One is a sharp impulsive later phase (denoted by SxS) at about 4 s after the direct S wave arrival (denoted by S). This phase is interpreted as the reflected S wave (SxS) from the midcrustal reflector existing in this area, as *Mizoue et al.* [1982] and *Horiuchi et al.* [1988] interpreted. For station GZD, particle velocity of this later phase is shown in Figure 4 for the time window displayed by solid bars below the seismogram. The particle velocity is dominant in horizontal

components, particularly in the NS component. This means the later phase can be identified as a wave that came to the station as an S wave. The other distinct later phase is again a sharp impulsive phase (denoted by SxP) at about 3 s after the direct S wave arrival. The particle velocity for this phase is dominant in the vertical component as shown in Figure 4. Thus this phase is a wave that arrived at the station as a P wave. Since these two later phases arrive after the direct S wave, wave types of these phases are interpreted as reflected phases from a certain velocity discontinuity rather than transmitted waves. The S wave that arrived at the station after the direct S wave is generated either by a reflection of the S wave at some velocity boundary (SxS) or by a reflection and P-to-S mode conversion at the boundary (PxS). Similarly, the P wave that arrived at the station after the direct S wave should be either a reflected P phase (PxP) or a reflected and S-to-P mode converted phase (SxP) from a subsurface reflector.

The later phase at about 4 s after the direct S wave cannot be interpreted as a reflected and P-to-S mode converted wave (PxS) but as a reflected S wave (SxS) as described below. If this phase is assumed to be an SxS wave, we can calculate theoretical
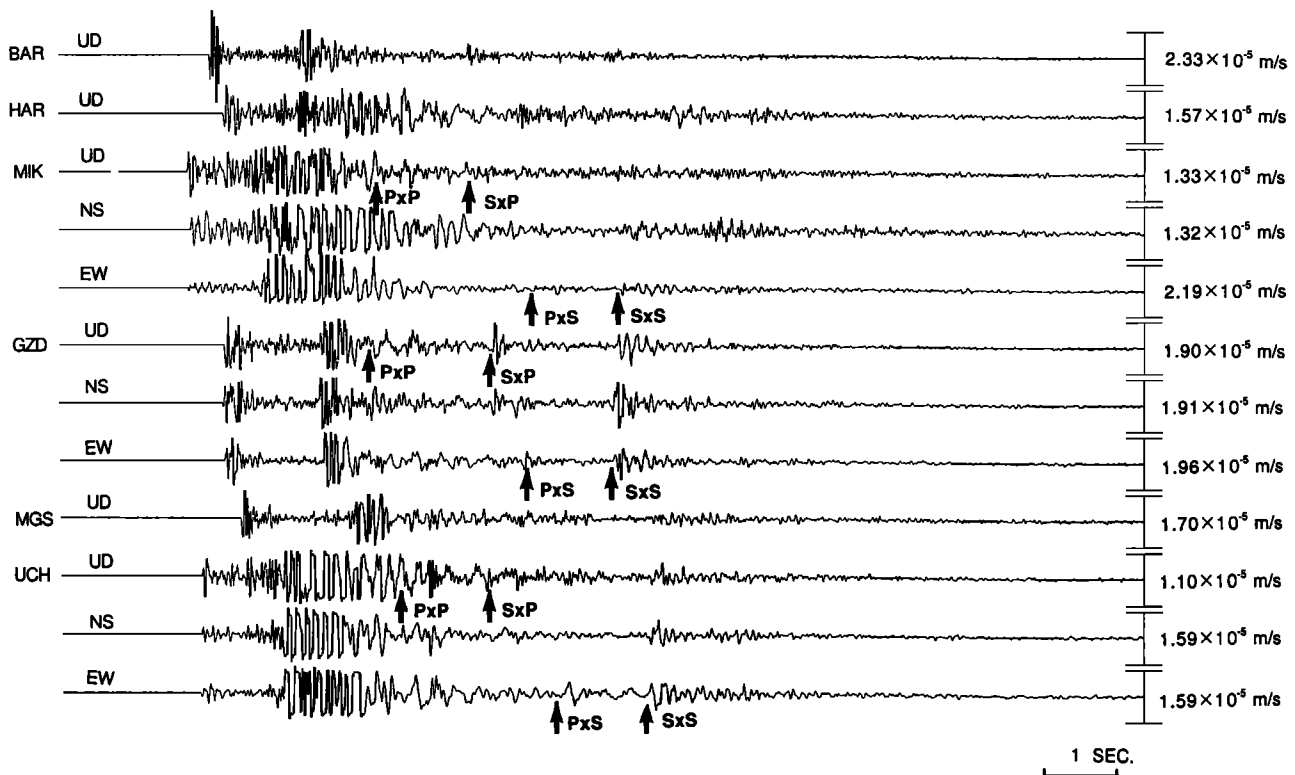
Figure 3. An example of seismograms showing clear later arrivals. Solid arrows point to the expected arrival times of PxP, PxS, SxP, and SxS waves from the reflector shown in Figure 9.

arrival times of other reflected phases by using the estimated location of the reflector from SxS arrival time. The calculated arrival times of SxP, PxS and PxP phases are shown by arrows below the seismogram in Figure 3 and 4. Although the location of the reflector is estimated only by SxS travel time, the distinct later phase at about 3 s after the direct S wave can be explained by the calculated SxP phase. Moreover, we can see a weak phase around the calculated PxP arrival time in the vertical component of the seismogram. Alternatively, if we interpret the later phase at about 4 s after the direct S wave as a PxS wave, we cannot explain the arrival times of the other later phases observed. Accordingly, we interpret the two distinct later phases as SxP and SxS waves. Small amplitudes of PxP and PxS phases are considered to be caused either by the physical property of the subsurface reflector or by the focal mechanism of the event. Distinct S wave reflection phases, identical to those shown in Figure 3, can be frequently detected at many of the stations in this area from the two groups of earthquakes. At several stations, however, the reflected phases are not observed. Stations at which the reflection phases cannot be detected are shown by station symbols with open circles in Figure 1. They are distributed at the northern and western edges of the present observation network. This systematic distribution in space roughly shows the extent of the subsurface reflector.

Geometry of the Reflector

In the earlier studies for mapping the midcrustal reflector, the shape of the reflector surface has been assumed to be a single horizontal plane [e.g., *Mizoue*, 1980; *Mizoue and Ishiketa*, 1988; *Mizoue et al.*, 1982; *Iwase et al.*; 1989] or a single inclined flat plane [*Horiuchi et al.*; 1988, *Inamori et al.*; 1992].

This assumption is not applicable if the reflector actually has a complicated shape with a curved surface, which seems to be quite probable in reality. In order to estimate the real shape of the reflector, we developed a method that minimizes the break of the single flat plane assumption. The basic idea of the method is to assume that the curved surface of the reflector is composed of many small planes, or in other words, the curved surface is approximated by a polyhedron.

Data presently used are arrival times of the SxS phase at each station from a series of earthquakes within a certain range of hypocenter locations. At some of the stations, the SxS phase can be seen but is not very clear. In such a case, we read SxS wave arrival times by drawing seismic sections in the same way as *Inamori et al.* [1992]. Horizontal component seismograms recorded at a station from many events are plotted in the order of their hypocenter locations after the automatic amplitude control (AAC) and the normal moveout (NMO) corrections are applied to the seismograms. An example of the seismic sections thus obtained is shown in Figure 5. The present processing, which is usually used in seismic reflection profilings, magnifies the amplitude in the S coda part of the seismogram to make up effects of seismic wave attenuation and geometrical spreading, and converts the time axis of the original seismograms to the depth axis. The depth axis corresponds to the depth of reflectors which are assumed as horizontal planes. By making seismic sections such as shown in Figure 5, we can easily identify the SxS phase. For instance, the SxS phase is continuously appearing from north to south at depths ranging from 14 to 17 km in the record section at station SKY, as can be seen in Figure 5. The seismic section shown in the figure indicates that the reflector is not horizontal but dips to the south.

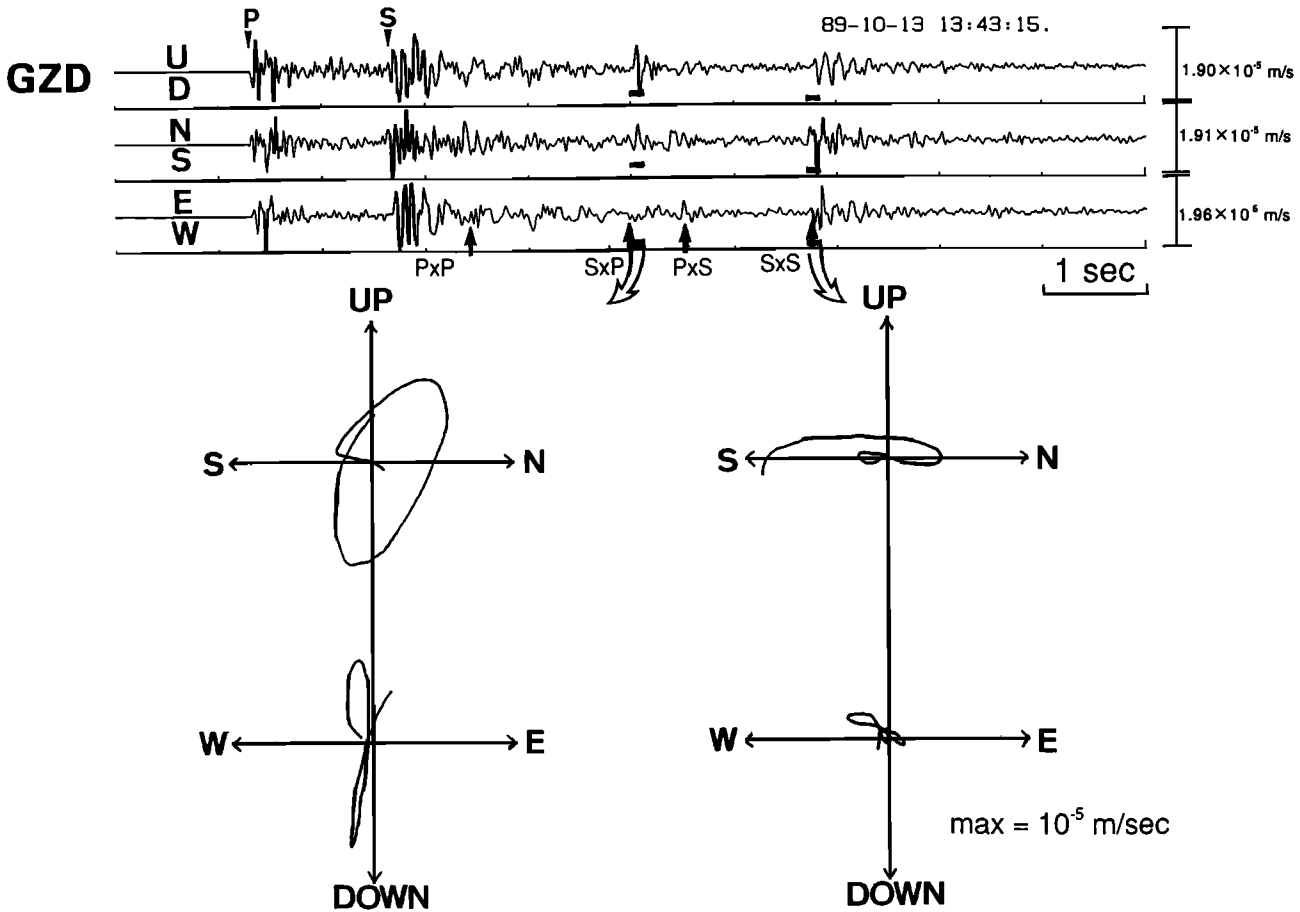For locating the top surface of the reflector, we assume here a

Figure 4. (Top) An example of three-component seismograms showing clear later arrivals. Solid arrows point to the expected arrival times of PxP, PxS, SxP and SxS waves from the reflector located in the next interval. (Bottom) Particle velocities of the two distinct later arrivals (SxP and SxS waves) for time windows displayed by solid.

constant S wave velocity above the reflector in the study area. The constant velocity model was adopted for determination the hypocenters by this seismic network [Ito et al.,1994]. Ito et al. [1994] showed that the accuracy of hypocenters determined by this network is better than 500 m in the horizontal direction and about 1 km in the vertical direction [Ito et al., 1994]. In a region at depths shallower than the maximum depth of earthquakes (about 12 km), this assumption does not make a severe error. Thus we assume the constant velocity model in this region rather than a complicated structure model for which we do not have any precise information at present. Let us consider a ray path of an SxS wave from a certain event to a station. The travel time of this wave is equal to that of an S wave propagating along a straight line connecting the hypocenter of the event to the image point of the station, as schematically shown in Figure 6. Next we consider another event whose location is close to the former event. If the reflector can be assumed as a single flat plane, the two reflection points are on the same single plane. Then the image point of the station for the ray from the s event coincides with that from the first event. If we have more than three events satisfying the above assumption, the image point of the station (hereafter referred to an image station) can be located from travel time data of the SxS waves from these events by using a nonlinear least squares method. The observation equation is written as

$$r_j^2 = \sum_{i=1}^{3} (x_{ij} - x_i)^2 \qquad j=j\text{th event, } i=1,2,3 \qquad (1)$$

where x_{ij} is the hypocenter location of the jth event in Cartesian coordinate system, x_i is the location of the image station, and r_j is the length of the ray path of the SxS wave from the jth event and is obtained from the observed SxS travel time and the S wave velocity model. This equation is solved by a modified Marquardt method.

The reflector plane is obtained by the location of image station ($\mathbf{x}_m$) and station ($\mathbf{o}$), where $\mathbf{x}_m$ and $\mathbf{o}$ are location vectors. Namely, the reflector plane contains a midpoint between the image station and the station and is orthogonal to a vector $\mathbf{x}_m - \mathbf{o}$. Locations of reflection points and a local strike and dip angle of the reflector can be determined from the locations of the station, the hypocenters, and the estimated image station. The present method assumes that the S wave velocity is constant in the study area and that the surface of the reflector is locally a single plane within a range where these reflection points are distributed. The latter hypothesis seems to hold to a fairly better approximation than that in the previous studies, since the range where reflection points are distributed for one station is much smaller than that for all stations. The total surface of a complicated-shaped reflector can be estimated
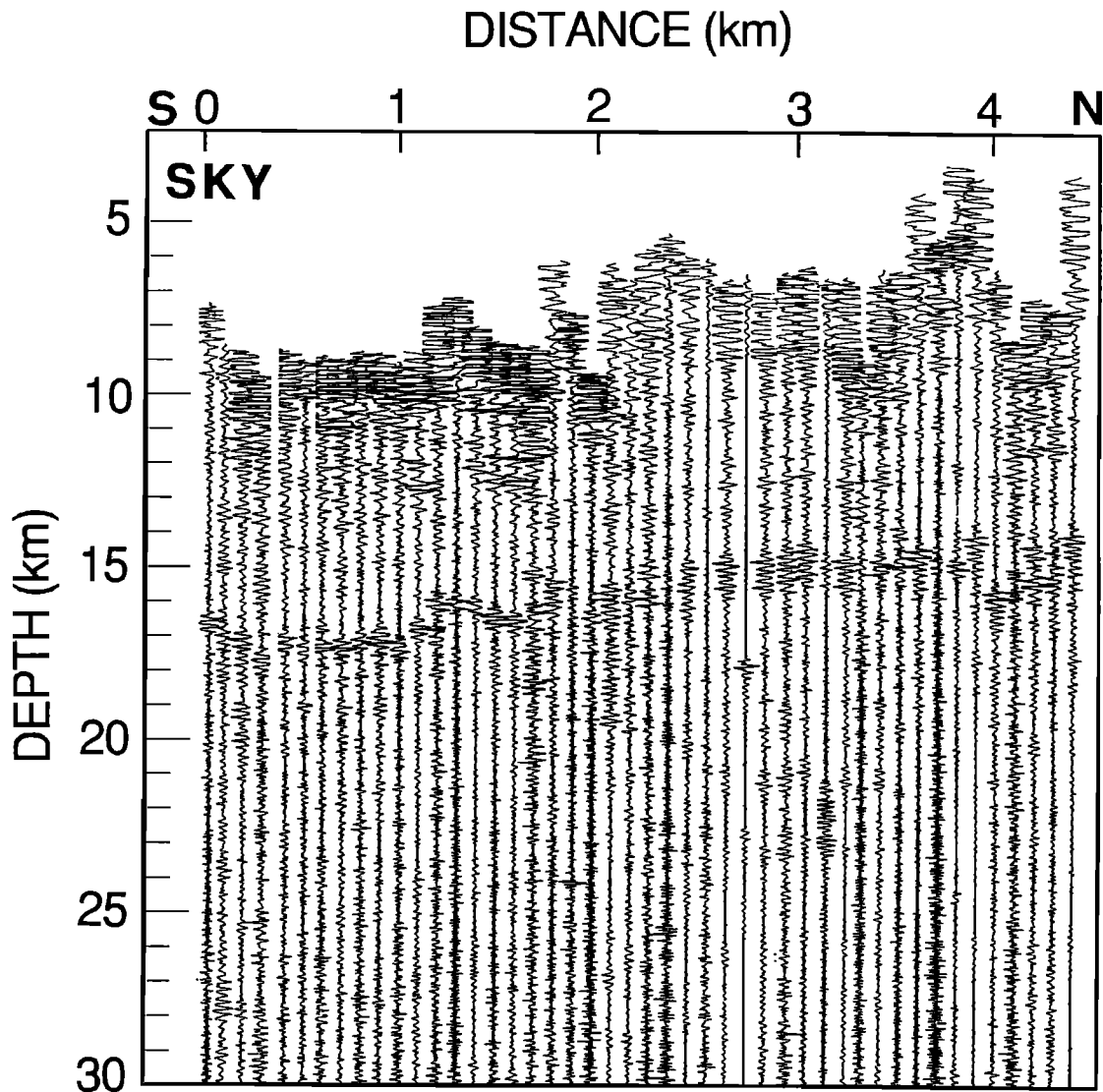
DISTANCE (km)

Figure 5. Horizontal- component record section at station SKY for earthquakes in the Ashio region. In each trace the time axis is converted to depth axis by normal moveout processing, and amplitudes of the *S* coda part are magnified by automatic amplitude control processing.

by putting together a set of small flat planes which are determined from different combinations of station and hypocenters. For the case that the reflector is actually composed of plural planes, this method is more effective to discriminate the planes rather than that in the previous studies.

The size of area, which is assumed to be a single plane, is prescribed by a spatial extent of hypocenters used in each inversion step. Although the resolution for mapping the total surface of a reflector becomes better with a narrower spatial extent of hypocenter distribution in each step, the extent of hypocenter distribution we can adopt is restricted by the accuracy of hypocenter locations and the number of earthquakes to reliably solve the image station inversion. Here we use two groups of earthquakes, one that occurred near Ashio and the other near Mt. Sukai. Both are spatially concentrated in each area, as mentioned before. Two image stations corresponding to the two groups of earthquakes can be calculated for each station,

if the *SxS* phases are identified at that station from the two earthquake groups. The local strike and dip angle of a small plane, estimated individually from the combination of a station and a group of events, are listed in Table 2 together with their estimation errors. Average depths and average depth errors of the reflection points estimated from the calculated location of the image station and from errors of the image station are also listed in the table. In this estimation *S* wave velocity is assumed to be 3.4 km/s, which is adopted in the hypocenter determination in this region [*Ito et al.*, 1994].

Figure 7 shows an example of the results of the inversion estimating the reflector by using the data at station SKY from the Ashio earthquake group. Hypocenters used in this case, estimated reflection points and rays of *SxS* waves are plotted on a horizontal map and NS and EW vertical cross sections. The reflection points, and the hypocenters are shown by crosses whose horizontal and vertical lengths indicate estimation errors.
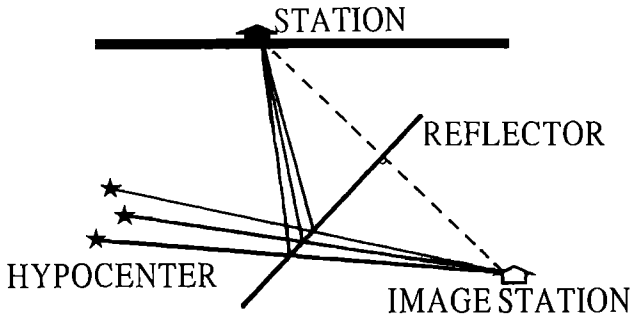
Figure 6. Schematic illustration of ray paths of SxS phases and the location of the image station with respect to the reflector.

The assumption that the reflector surface is locally a single flat plane should be satisfied in the range where the reflection points are distributing. All of the reflection points calculated from the image stations listed in Table 2 are plotted by crosses in Figure 8. Horizontal and vertical lengths of the crosses on the reflection points denote their estimation errors. After removing the reflection points with estimation errors larger than 3 km, we show the reflection point distribution in Figure 9. In the map view, estimation errors of the local strike of the reflector are displayed on the reflection points instead of horizontal location errors of the reflection points. As can be seen from this figure, the reflection points are distributed over an area of about 15 km x 15 km in a depth range from about 8 to 15 km. The total distribution of these points has a conical shape shallowing toward the location of Nikko-Shirane volcano, which is shown by a solid triangle in the figure. Based on the locations of the estimated reflection points, we infer the geometry of the subsurface reflector as plotted by contour lines in the figure. Taking into account the estimation errors of the reflection points, it is difficult to determine whether these reflection points with a conical shaped distribution are on a continuous single-reflector plane or are on many different small reflector planes. In any case, there exists a reflector body having a conical shape shallowing to the north beneath this region: the body has a single very reflective surface or contains many reflective planes within it.

A group of reflection points in the southwestern end has a different trend of dip angle and dip direction from that of the main group forming the conical shape. This suggests the existence of a different reflector surface. This reflector is nearly horizontal at a depth of about 16 km and is distributed over an area of about 4 km x 3 km located at the southwestern end of the distribution of the reflection points.

Internal Structure of the Reflector

As can be seen from an example of SxS seismograms (figure 3 and 4), the SxS wave has a very large amplitude. In some cases, its amplitude is even larger than that of a direct S wave. This implies that the reflector has a very large reflection coefficient. On the other hand, frequency dependence of reflection coefficient is directly influenced by internal structure of the reflector. Here, we investigate SxS wave amplitude and try to estimate the reflection coefficient as a function of frequency from the observed spectra of SxS waves.

In general, amplitude of direct S waves from the ith earthquake observed at jth station at frequency f Hz can be

$$A_{ij}(f) = S_i(f)I_j(f,\theta)F_{ij}/r_{ij}\exp(-2\pi f t_{ij}Q^{-1}) \qquad (2)$$

where $S_i(f)$ is source spectrum of the ith event, F_{ij} is the factor of radiation pattern at jth station, $I_j(f,\theta)$ is the station factor of jth station including instrumental response, site amplification factor and free surface effect, θ is an incident angle to the surface which can be calculated from homogeneous half space, t_{ij} and r_{ij} denote travel time of direct S wave and geometrical spreading factor, respectively, and Q^{-1} is attenuation factor along the ray path, which is assumed as a constant value. Amplitude of the SxS wave with an incident angle α to the reflector at frequency f Hz is expressed by the following formula:

$$A_{refij}(f) = S_i(f)I_j(f,\theta')F_{ij}'/r_{ij}'\exp(-2\pi f t'_{ij}Q^{-1})R(f,\alpha) \qquad (3)$$

where $R(f,\alpha)$ is a reflection coefficient, r_{ij}' is the geometrical spreading factor of the SxS wave, calculated from a distance between the ith hypocenter and the image point of jth station in the present analysis, t'_{ij} is travel time of the SxS wave from the ith event to the jth station. To remove the effect of the source factor, we take the amplitude ratio of $A_{refij}(f)$ and $A_{ij}(f)$. Then

$$A_{refij}(f)/A_{ij}(f) = I_j(f,\theta')/I_j(f,\theta)F_{ij}'/F_{ij}r_{ij}$$
$$/r_{ij}'\exp(-2\pi f(t'_{ij}-t_{ij})Q^{-1})R(f,\alpha) \qquad (4)$$

First, we investigate amplitude ratios taken from band-pass filtered seismograms. Figure 10 shows ratios of root-mean-square amplitude of the SxS wave to that of the direct S wave plotted against incident angle of SxS wave to the reflector. The ratios plotted here are obtained from seismograms observed at

Table 2. Estimated Location of the Midcrustal S Wave Reflector at Each Station

Station	region	AZ	δAZ	Dip	δDip	$\overline{z}$	δZ	No.ev
MJN	S	-7.9	14.5	36.4	5.0	9.3	1.2	30
KST	S	-88.8	6.7	51.5	18.7	8.1	3.5	16
YNG	S	6.5	44.5	21.1	5.0	11.1	1.3	14
SJH	S	-	-	-	-	-	-	5
BAR	A	-	-	-	-	-	-	4
HAR	A	-	-	-	-	-	-	5
MIK	A	-38.1	3.4	38.2	2.4	13.3	0.7	11
GZD	A	-25.1	3.8	36.1	3.1	12.7	0.8	14
	S	5.1	23.3	36.8	5.3	11.3	1.4	11
MGS	A	-24.8	2.8	31.6	1.5	13.2	0.3	11
UCH	A	-29.7	3.2	38.8	2.4	13.5	0.7	12
KMT	S	-27.9	24.6	4.15	1.0	16.7	0.2	96
	A	32.5	21.1	11.9	2.8	16.2	0.5	52
SKZ	S	-86.2	53.8	1.35	1.0	15.5	0.1	40
	A	-12.6	4.7	16.9	1.1	13.8	0.6	20
SKY	S	7.7	8.1	21.4	13.4	14.3	1.5	46
	A	-3.7	1.0	49.7	1.3	9.4	0.3	41
MRY	A	-1.6	1.7	39.1	1.6	9.7	0.4	24
	S	NC	NC	NC	NC	NC	NC	48

AZ and Dip are the azimuth and dip angle of the steepest ascending vector on the reflector in degrees. $\overline{z}$ denotes average depth of reflection points in km. Parameters with d denote estimation errors. No.ev is the number of earthquakes used in the image station inversion. Earthquakes used are those in the Mt. Sukai group and in the Ashio group, and are indicated by region codes S and A, respectively. Dash indicates small number of data; NC, not converged.
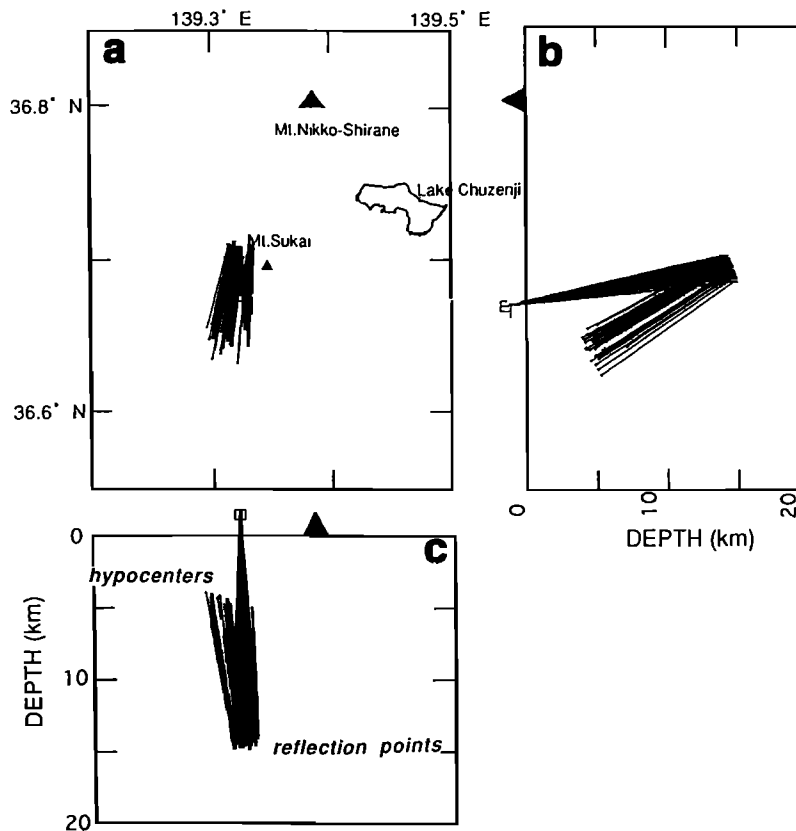
Figure 7. Locations of estimated reflection points and earthquakes used in the image station inversion at SKY for the Ashio earthquake group. (a) horizontal, (b) N-S, and (c) E-W vertical cross sections. Length of each cross symbol showing reflection points and earthquakes denotes spatial error. Solid lines connected from hypocenters to stations via reflection points are ray paths of SxS waves. Open square shows the location of station SKY.

GZD, MIK, and SKY, which have relatively large amplitudes of SxS waves compared with the other stations. The root-mean-square amplitude is calculated from a data window of 1 s of band-pass filtered seismograms at 12 Hz, which is the predominant frequency both for SxS and S waves. Based on a constant velocity structure model, corrections for geometrical spreading factors of SxS and S waves are made for calculating these amplitude ratios. Magnitudes of most earthquakes used are not large enough to uniquely determine their focal mechanisms, but mechanism solutions of some events are obtained. Corrections for the effect of radiation pattern are made for those events (shown by solid stars in Figure 10). Rays of SxS waves are calculated from the location and geometry of the reflector determined in the previous section. After correcting the radiation pattern, scattering of the ratios becomes small. According to equation (4), the root-mean-square amplitude ratio shown in the figure corresponds to reflection coefficient if we can assume $Q^{-1}=0$ and $I_j(f,\theta')/I_j(f,\theta)=1$. Figure 10 indicates that the reflection coefficient of the reflector beneath Nikko-Shirane volcano is close to 1 at 12 Hz and slightly decreases with increasing incident angle. Some of the observed amplitude ratios have values greater than 1. Since reflection coefficient theoretically cannot exceed 1, this means that estimation errors of these values are not very good. The scatter in the observed ratios is mainly caused by the effect of radiation pattern and site factor. Some of the observed ratios exceed 1 even after the correction for the effect of radiation pattern, which indicates

that the site effect has an angular dependency (namely, $I_j(f,\theta')/I_j(f,\theta) \neq 1$) and/or that the correction for radiation pattern is not sufficient due to the estimation error of focal mechanism solutions. In any case, the average value of the observed amplitude ratios is very large, although they are widely scattered. Such large-amplitude ratios suggest that the reflector has a strong velocity contrast with the overlying crustal rock. This large velocity contrast leads us to imagine that the reflector contains a fluid material.

In order to obtain the information on the internal structure of the reflector body, we investigate a spectral ratio of SxS wave to direct S wave. As can be seen from equation (4), the frequency dependence of the spectral ratio is in proportion to the frequency dependence of reflection coefficient of the reflector. However, the spectral ratio is affected also by site amplification factor just beneath a station if the amplification factor strongly depends on incident angle and/or azimuth of hypocenter of S wave to the surface. We cannot reject a possibility of some amount of angular dependency of the site amplification factor as described above. We checked the dependency of site effect on both azimuth of hypocenter and incident angle by taking direct S wave spectra. Roughness of the spectra implies frequency dependence of the site effect if corner frequencies of earthquakes are higher than the target frequency band in our analysis.

Figure 11 shows spectra of direct S waves for a 1-s time window from direct S wave arrival. Spectra of direct S waves for various azimuths (86°-150°) with a fixed incident angle of about
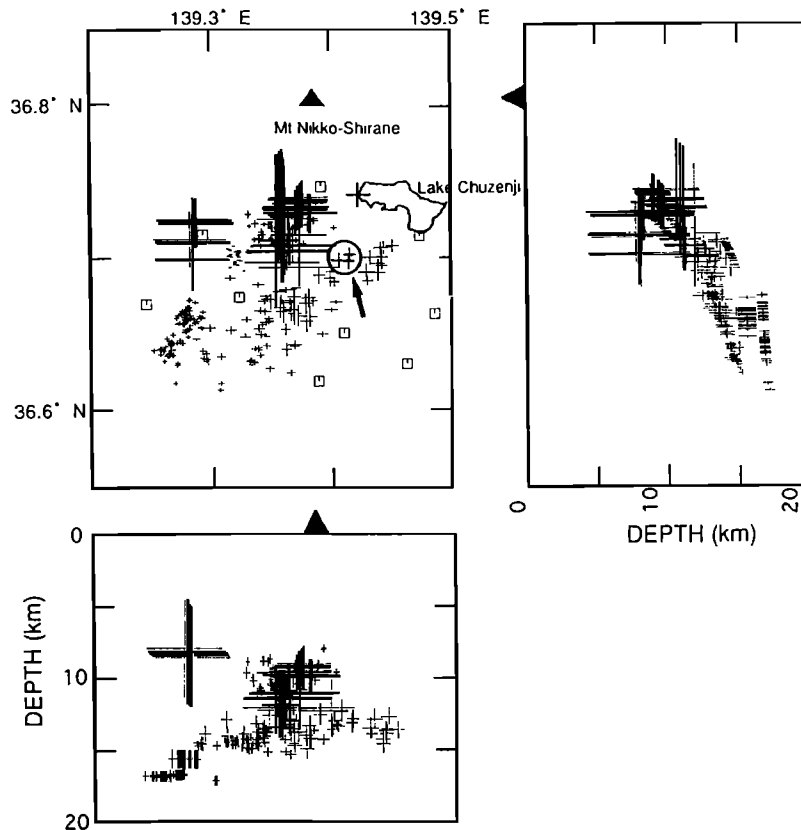
Figure 8. Spatial distribution of reflection points estimated from all stations using the two earthquake groups. Length of each cross symbol showing reflection points denotes estimation error. Open squares in the horizontal map show the locations of stations used. Crosses enclosed by an open circle with an arrow pointing to it are epicenters for earthquakes used in the spectral ratio analysis.

23° are plotted in Figure 11a. The spectra displayed here have similar shapes. Local peak frequencies of these spectra do not change very much for the large azimuthal variation. This suggests that azimuthal dependency of site effect is negligible. On the other hand, discrepancy of site effect between different incident angles is serious. Figure 11b shows spectra of direct *S* waves with various incident angles (20°- 65°) and with a nearly constant azimuth (about 10°). The shape of the spectra becomes rough with increasing incident angle. Moreover, the peak frequency of the spectra at lower incident angles is quite different from that at higher incident angles. It is difficult to explain this discrepancy if corner frequencies are in the range shown in the figure. Taking the spectral ratio of *SxS* to direct *S* waves having different incident angles from each other will cause a wrong estimation of the internal structure of the reflector. In such a case, practically, the estimated ratio contains an error of more than a factor of 2. This suggests that a large scattering of amplitude ratios in Figure 10 is partially attributed to the dependence of site effect on incident angle. In order to avoid the effect of different site amplification factors between direct *S* waves and *SxS* waves caused by their angular dependency, we take the spectral ratio by using direct *S* waves and *SxS* waves whose incident angles are similar to each other. moreover, it is important to use data whose signal-to-noise (S/N) are high enough in a wide frequency range to get the information of the internal structure of the reflector. In the present analysis, we selected seismograms from six events observed at station GZD. incident angles of direct *S* and *SxS* waves are similar to each

other (incident angle differences |θ-θ'|<1°) for these events, and *SxS* waves appear very clearly at this station with high S/N ratios compared with those at the other stations.

Figure 12a shows an example of seismograms recorded at GZD. Horizontal particle velocities in radial (SV) and transverse (SH) components to the ray are synthesized from seismograms in NS and EW components. In the earlier part of the seismogram, both the SV and SH components are calculated from the locations of hypocenter and station. On the other hand, these components in the later part are calculated from the locations of reflection point of *SxS* wave and station. Incident angles of both *S* and *SxS* waves shown in Figure 12a are 22.4°. Spectral ratio is obtained from an amplitude spectrum of *SxS* waves divided by that of direct *S* waves. In order to avoid the difference of site effects between SV and SH directions, amplitude spectra of *SxS* waves in the SH and SV components are divided by those of direct *S* waves in the SH and SV components, respectively. Figure 12b shows the amplitude spectra of direct *S* and *SxS* waves and the amplitude spectral ratio. Those for SV and SH components are shown on the left- and right-hand sides, respectively. We can see several peaks in the spectral ratios. In this study we discuss the internal structure of the reflector body based on the ratio of SH component because usually the site effect of the SH component is simpler than that of the SV component. The site factor of the SV component is disturbed by the energy of the *S*-to-*P* mode converted wave at the free surface in a layered structure, and thus it presents a complicated feature. The observed spectral ratios are stacked to improve the
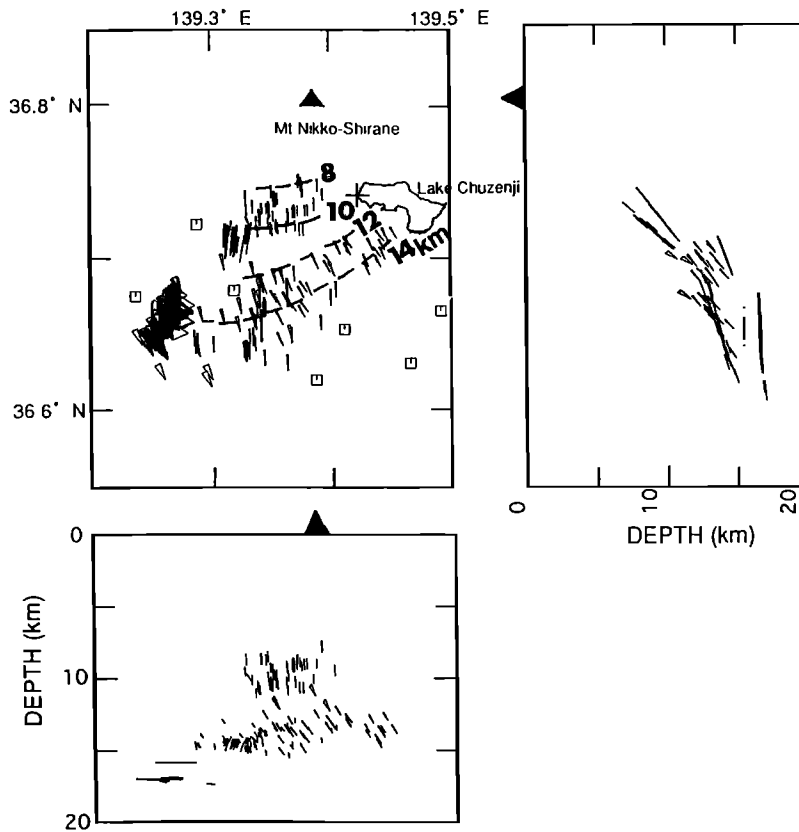
Figure 9. Spatial distribution of reflection points with estimation errors less than 2 km. Local upgrade direction and angle of the reflector, together with their estimation errors, are shown at each reflection point. In the horizontal map estimation errors in azimuth are shown by the angles of fan-shaped symbols. Estimation errors in dip angle are projected on the vertical sections again by the angles of fan-shaped symbols. Other symbols are the same as in Figure 8.

estimation. The SxS waves presently selected have incident angles similar to those of the reflector (17°-18°). Map and vertical cross-sectional views of hypocenters, reflection points and ray paths of SxS waves selected here are also shown pointing to it in Figure 8. The hypocenters are enclosed by a circle with an arrow pointing to it in Figure 8. The internal structure of the reflector presently investigated is for its narrow portion, where these reflection points are distributed.

We stacked the observed spectral ratios at GZD for the six selected events. Each spectral ratio is stacked after removing its average offset value. The stacked spectral ratio, shown in Figure 13, indicates that several peaks appear at different frequencies. If examined in more detail, we can see that relatively large peaks repeatedly appear at an interval of about 13 Hz. In addition, it seems that there exist repeated small peaks with an interval of about 4 Hz, and these are superimposed on the large repeated peaks with an interval of about 13 Hz. Equation (4) shows that parameters having frequency dependencies are the site amplification factor $I_j (f,\theta')/I_j (f,\theta)$, the attenuation factor exp ($-2\pi f(t_y' - t_y)Q^{-1}$), and the reflection coefficient $R(f,\alpha)$. In the present case, $I_j (f,\theta')/I_j (f,\theta)$ is considered to be very close to 1 because we selected data with very small values of $|\theta-\theta'|$. The stacked spectral ratio does not have any systematic tendency to decrease with increasing frequency, which suggests that the effect of the attenuation factor can be neglected. Consequently, we can assume that the frequency variation of the observed spectral ratio reflects the frequency dependence of the reflection

coefficient $R(f,\alpha)$. We discuss here only the frequency dependence of the observed spectral ratio and not its absolute value because it has an offset value due to the factor of the radiation pattern F_y'/F_y, which is independent of frequency.

In the next step, we try to find a model for the internal structure of the reflector body, which explains the frequency dependence of the observed spectral ratio, by using a grid searching technique. We assume that the reflector body is composed of one layer or of a few layers. Parameters characterizing the reflector body are P and S wave velocities, density, and layer thickness. They are assumed to be constant in each layer. We should take into account the observed duration time of SxS waves for searching the physical parameters of the reflector body. As can be seen from Figure 3 or Figure 13, oscillations of SxS waves continue for about 1 s. Duration times of earthquake sources are much shorter than 1 s, since the earthquakes used here have magnitudes less than 2.5. The observed duration of the SxS phase is caused by site resonance and/or by propagation time of SxS waves within the reflector body. moreover the time window of 1 s was taken for calculating the spectral ratio. Therefore we can only estimate the internal structure of the reflector body corresponding to at most 1 s of propagation time: the deeper portion which corresponds to more than 1 s of propagation time cannot be detected by the present analysis. The appearance of several peaks in the observed spectral ratio implies that S wave velocity is not zero in the reflector body. In other words, the reflector is not composed of pure liquid like a magma or water. If
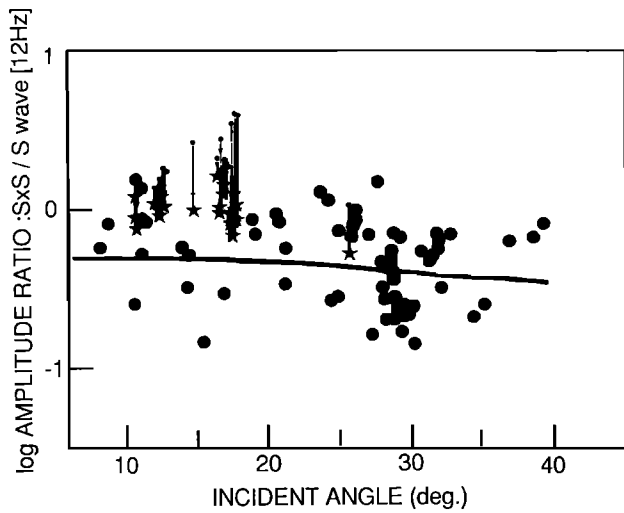
Figure 10. Root-mean-square amplitude ratios of SxS to direct S waves at 12 Hz for 1 s time windows. Stars show the ratio for which corrections for the radiation pattern from the source are made. Lengths of arrows connected to stars denote amounts of the correction for radiation pattern. Small solid circles show the ratio for which radiation pattern is not corrected. Solid line shows the theoretical value calculated from the model shown in Figure 16.

S wave velocity is equal to 0, which was seen in the result by *Ake and Sanford* [1988] in the Rio Grande Rift, frequency dependence of the reflection coefficient for S waves should not exist, and the frequency peaks do not appear. Therefore it is considered that the reflector body beneath Nikko-Shirane volcano partially contains liquid materials.

We assume the layered structure of the reflector body surrounded by the matrix medium with S wave velocity V_{s0}=3.4

km/s. The effective parameters on the S wave reflection coefficient of the reflector are S wave velocity V_s, density ρ, and layer thickness h. For simplicity, ρ is assumed to be constant (ρ =2.7x10³ kg/m³), since, the value of V_s changes drastically with varying fraction of liquid inclusion compared with density value [*Murase and McBirney*, 1973]. In the case of an n-layer model, various values of S wave velocity V_{si} and thickness h_i of ith layer (i=1,2,...,n) of the reflector body are given within a certain range as

$$V_{si}=V_{s0}+dV_{si}(j\text{-}1)\ j=1,2,3,...,\ J \tag{5}$$

$$h_i=h_{i0}+dh_i(k\text{-}1)\ k=1,2,3,...,\ K \tag{6}$$

For each step of i, j, and k, the frequency dependence of the S wave reflection coefficient is calculated by using the method of *Kennett and Kerry* [1979]. By calculating a correlation coefficient between the theoretical reflection coefficient thus obtained and that observed one shown in Figure 13, we determine a model that has the maximum correlation coefficient in a certain range of V_{si} and h_i values. The range is taken under the condition of the detectable range of propagation time within the reflector body. Practically, we take V_{si} and h_i values in the range satisfying the following relation:

$$t=\sum_{i=1}^{n}\frac{h_i}{V_{si}\sqrt{1\text{-}(pV_{si})^2}}<1 \tag{7}$$

where p is a ray parameter of the S wave (p=sin α/V_{s0}).

First, we discuss a single-layer model. medium parameters V_{s10}, dV_{s1}, h_{10} and dh_1 in the formula (5) and (6) were set at 0.1, 0.1, 0.001, and 0.002, respectively. The numbers of steps for velocity (J) and thickness (K) are 35 and 875, respectively. Cases with correlation coefficients higher than 80% of the
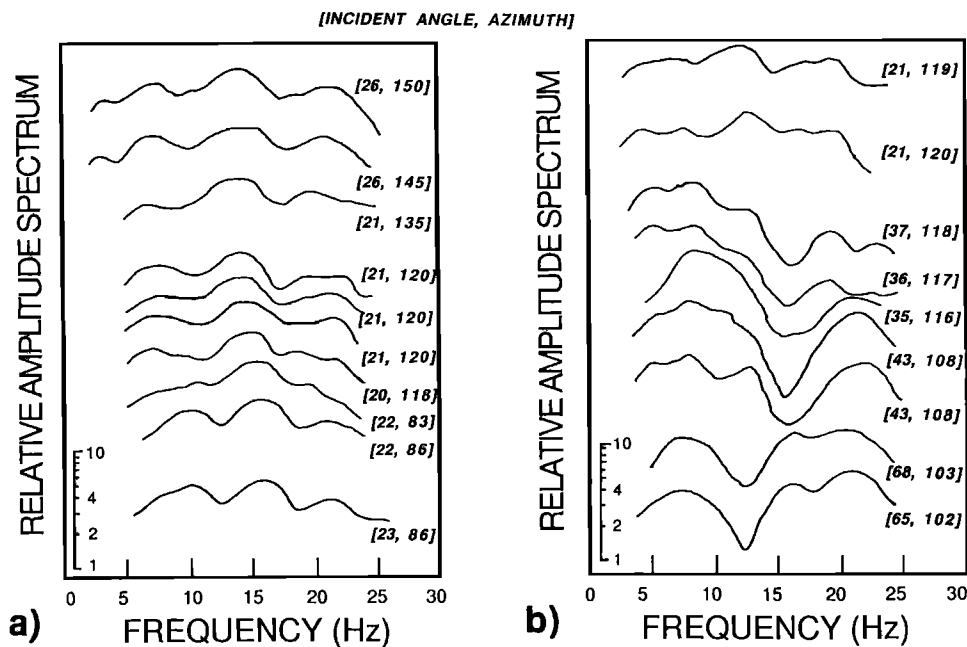
[INCIDENT ANGLE, AZIMUTH]

Figure 11. Amplitude spectra of direct S waves at GZD. Spectra are plotted for (a) variable azimuths with a fixed incident angle and (b) variable incident angles with a fixed azimuth. Numbers enclosed by brackets denote incident angles to free surface and azimuths from the station.
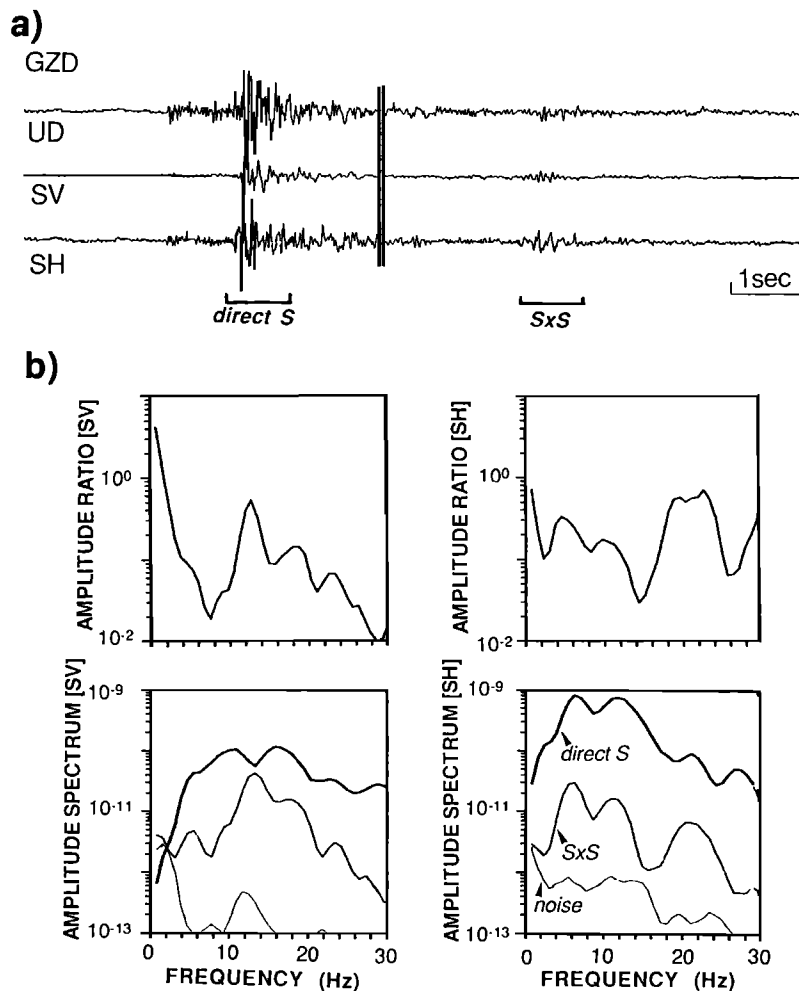
Figure 12. (a) Three-component seismogram at GZD. The horizontal components are synthesized to make SV and SH components for the direct S wave in the earlier part of the seismogram and to make SV and SH components for the SxS wave in the later part, respectively. b) Amplitude spectral ratio of SxS wave to direct S wave. Amplitude spectra of direct S wave, SxS wave and noise are also shown at the bottom. SV and SH components are separately shown on the left and the right, respectively.

maximum correlation coefficient are shown by triangles on the V_{sl}-h_l plane in Figure 14. High correlation values are distributed around V_{sl} /h_l=25. In general, peaks of the reflection coefficient appear at frequencies of V_{sl} /h_l(2m+1), where m=0,1,2..., for the case of vertical incidence to a single-layer reflector body. This means that the correlation coefficient is insensitive to individual variations of V_{sl} and h_l under the condition of V_{sl} /h_l=const.

Figure 15 shows the calculated reflection coefficient having the largest correlation coefficient for the single-layer model. The observed reflection coefficient is also shown by a broken line. The maximum correlation coefficient is 0.6. In this model the thickness of the reflector body is only 115 m. All cases having correlation coefficients higher than 80% of the maximum correlation coefficient show that the reflector body is very thin and the layer thickness is equal to or less than the order of 100 m.

As previously mentioned, the stacked spectral ratio has large and small repeated peaks with frequency intervals of 13 Hz and 4 Hz, respectively. Although the single-layer model explains the major repeated peaks, the model cannot fit the minor peaks

because the reflection coefficient for a single-layer model essentially has repeated peaks with one frequency interval. In order to explain two kinds of repeated peaks, we have to consider at least a two-layer model. In order to get a better fitting to the observation, we investigate a two-layer model. Various values of medium parameters for each layer are taken for calculating the reflection coefficient, in a similar way to the case of the single-layer model. However, S wave velocity and thickness are taken at coarse steps in order to save computation time. For both layers (i=1,2), velocity and thickness are set at V_{si}=0.1+0.2(j-1), (j=1,2,...,17) and h_i=0.001+0.004(k-1), (k=1,2,...,437), respectively. Figure 16 shows the best fit model to the observed data. The maximum value of correlation coefficient is 0.74. The thicknesses of the first and s layers are 57 m with V_{sl}=2.3 km/s and 41 m with V_{s2}=1.1 km/s, respectively. In this model again, the total layer thickness of the reflector body is still thin (about 100 m). The s layer with an extremely low S wave velocity contributes to make the major repeated peaks with a frequency interval of about 13 Hz. The peaks with the shorter intervals are generated by the first layer. The calculated shape of the reflection coefficient for this model
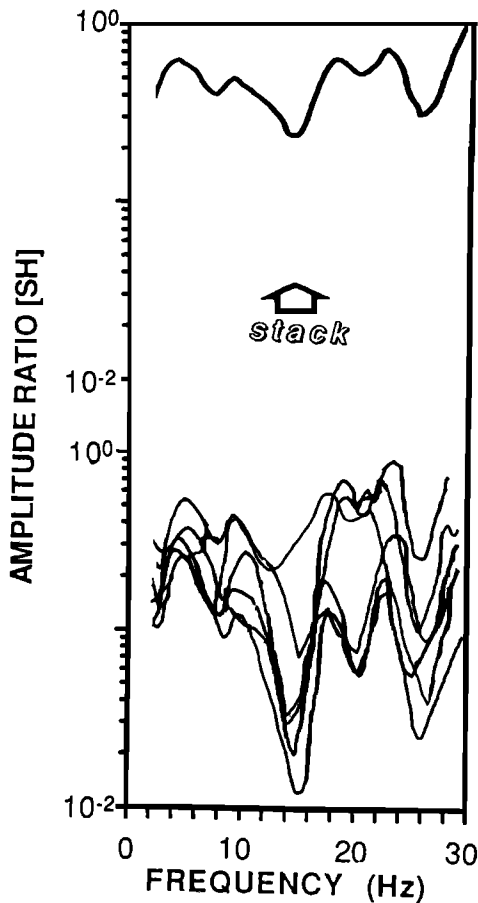
Figure 13. Amplitude spectral ratios of SxS to direct S waves at GZD for the seven events enclosed by a circle with an arrow pointing to it in Figure 8. Stacked spectral ratios from the six events are shown at the top of the figure.

is not different from that for the case in which the medium parameters in the first and second layers are exchanged.

Values of correlation coefficients higher than 80% of the maximum value are plotted on V_{s1}-h_1 and on V_{s2}-h_2 planes by triangles in Figure 17. The variation of correlation coefficients for the first layer is plotted in Figure 17a for the case of V_{s2}=1.1 km/s and h_2=41 m. In Figure 17b, the correlation coefficients for the second layer are plotted when the medium parameters in the first layer are fixed at V_{s1}=2.3 km/s and h_1=57 m. High correlation coefficients concentrate around V_{si}/h_i=const for both layers: for the first layer, V_{s1}/h_1~40, and for the second layer, V_{s2}/$h2$~26.

Based on the comparison between the observed and calculated reflection coefficients described above, we may conclude about the internal structure of the reflector as follows.

1. The reflector body is composed of at least two-layers and their V_{si}/h_i values are about 26 and 40 in order to explain the observed spectral ratio.
2. According to the best fitting model shown in Figure 16, the total thickness of the reflector body is about 100 m, and S wave velocity in it is quite low.

The theoretical reflection coefficients at 12 Hz calculated from the best fit model are plotted by the solid line in Figure 10. As described above, the final model is estimated by fitting the shape of spectral ratio of the SxS wave to direct S wave, and so we cannot discuss the absolute value of the reflection coefficient.

Yet we can see from this figure that the present model can roughly explain the observed data. Some differences existing between the theoretical value and observed amplitude ratio are considered to be caused by several factors. One major possible cause is the discrepancy of site effect between SxS and direct S waves. Plotted values in Figure 10 are not always estimated from SxS and S waves with the same incident angle. Then the amplitude ratio would scatter more than a factor of 2 from the actual reflection coefficient of the reflector. Another cause is the estimation error for radiation pattern. The correction for radiation pattern is not sufficient due to the estimation error of focal mechanism solutions. A large change of amplitude ratio will occur if P, T, and b axes of focal mechanisms change slightly.

Discussion and Conclusions

The presently estimated S wave reflector has a conical shape, and the reflection points are distributed to the south of Nikko-Shirane volcano as shown in Figure 9. Remarkable SxS phases were not observed at most of the stations set up at the northern and western edges of the seismic network. The reasons why the SxS phases do not appear at those stations may be (1) the reflector does not exist in the northward and westward extensions of the presently mapped reflector, (2) the reflector actually exists but SxS waves cannot reach those stations because of an unsuitable geometrical relationship among the stations, the reflector, and the hypocenters of shallow events in this area, (3) the reflector does not have a relatively wide and smooth surface but has a rough surface forming randomly oriented scatterers such as cracks, or (4) SxS waves do not have
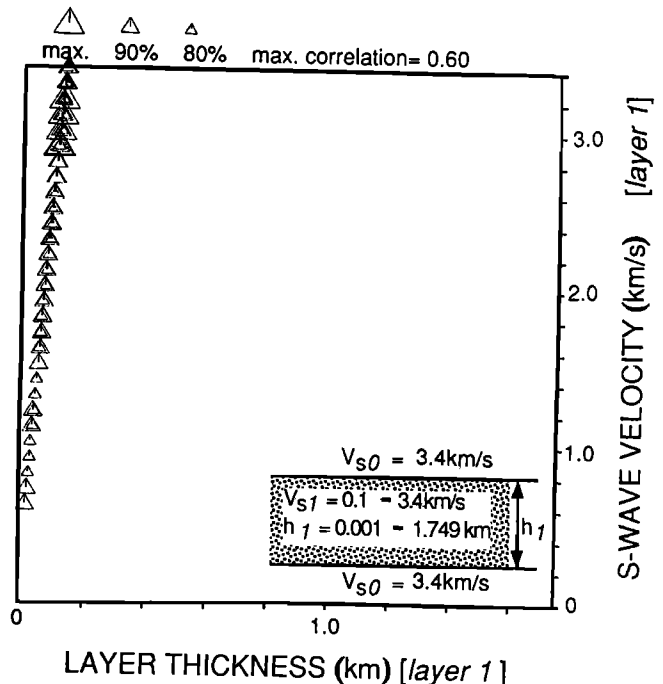

Figure 14. Distribution of correlation coefficient between the calculated and the observed reflection coefficient for a single-layer model. Correlation coefficients with values higher than 80% of the maximum value are plotted by triangles on the $Vs1$-$h1$ plane. Values of correlation coefficient are shown by the size of the triangle symbol (scale is shown at the top of the figure).

structure model

$$V_{S0} = 3.4km/s$$

$V_{S1} = 2.9 \, km/s$
$h_1 = 0.115 \, km$

h_1

$$V_{S0} = 3.4km/s$$

max. correlation : 0.6

model

observed

REFLECTION COEFFICIENT [SH-SH]

10^0

10^{-1}
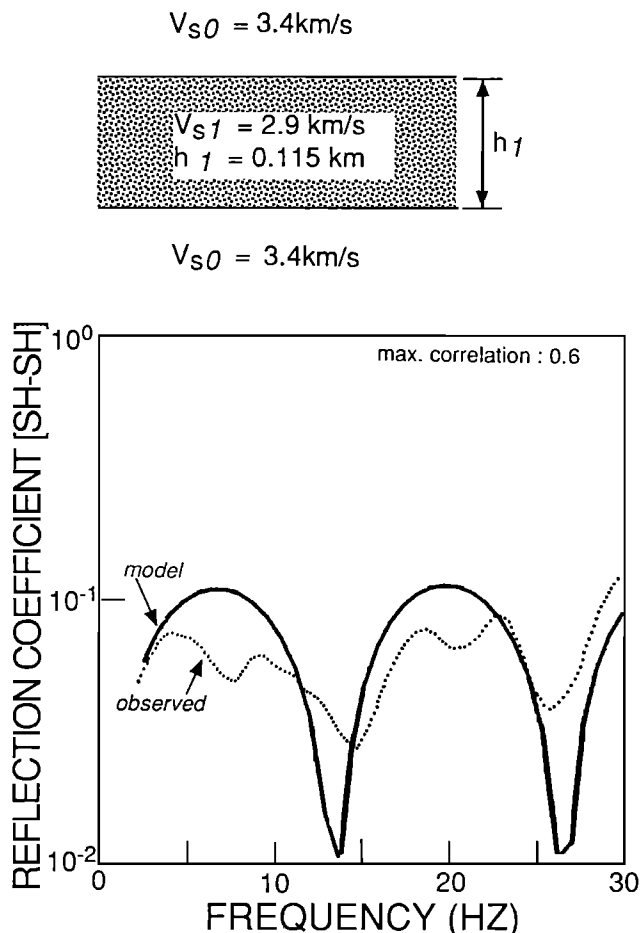
10^{-2}

0   10   20   30

FREQUENCY (HZ)

Figure 15. (Top) Best fit velocity structure for a single-layer model and (bottom) calculated reflection coefficient from the model (solid line) and from observations one (dotted line).

sufficiently large amplitudes due to the small reflection coefficient of the existing reflector and/or radiation pattern effect, and are concealed by S coda waves randomly scattered by inhomogeneity in the crust. It is difficult from the present data to determine which is the actual case.

The midcrustal S wave reflector beneath Nikko-Shirane volcano is estimated here to be composed of two very thin layers (0.041, 0.057 km) with a total thickness of about 0.1 km and with low S wave velocities. This suggests that the reflector body contains in it a liquid material such as a magma or water. The present result is similar to that obtained by Ake and Sanford [1988] for the midcrustal reflector existing beneath the central Rio Grande Rift near Socorro. They estimated the internal structure of the reflector body by fitting the whole shape of PxP waveforms to a multilayer model. Their result shows that S wave velocity is zero in the reflector body. This means that the reflector in the Rio Grande Rift is composed of liquid materials. On the other hand, S wave velocity is not zero in the reflector beneath Nikko-Shirane volcano, since the observed reflection coefficient shows a frequency dependence. This suggests that the fluid fraction in the reflector beneath the Nikko area is lower than that beneath the Rio Grande Rift.

Figure 18 shows an NS vertical cross section of earthquakes (open circles) in the Nikko-Ashio area. The presently estimated

location of the midcrustal reflector is also shown. The lower limit of earthquakes becomes shallow towards Nikko-Shirane volcano which is shown by a solid triangle at the top of the figure.

The reflector also shallows towards the volcano, being nearly parallel to the cutoff depth for the shallow earthquakes. The close geometrical relationship between the midcrustal reflector and the cutoff depth of shallow seismicity, similar to the present case, has been observed in the focal area of the 1984 Western Nagano Earthquake near Ontake volcano [Mizoue and Ishiketa, 1988; Inamori et al., 1992] and in the focal area of the Matsushiro earthquake swarm, as shown in Figure 19.

In the case of the Western Nagano Earthquake, the lower band of aftershocks shoals to the west. The shallower reflector of S waves, of the two, is nearly parallel to and 2-3 km apart from the cutoff depth for the aftershocks (Figure 19a). The midcrustal S wave reflector detected by Nishiwaki et al. [1989] below the Matsushiro earthquake swarm becomes shallow to the northeast and is again nearly parallel to the cutoff depth for the swarm events (Figure 19b). These observations suggest that the existence of the midcrustal S wave reflector controls the cutoff depth for shallow seismicity which can be interpreted as the depth to the brittle to ductile transition zone or stick-slip to
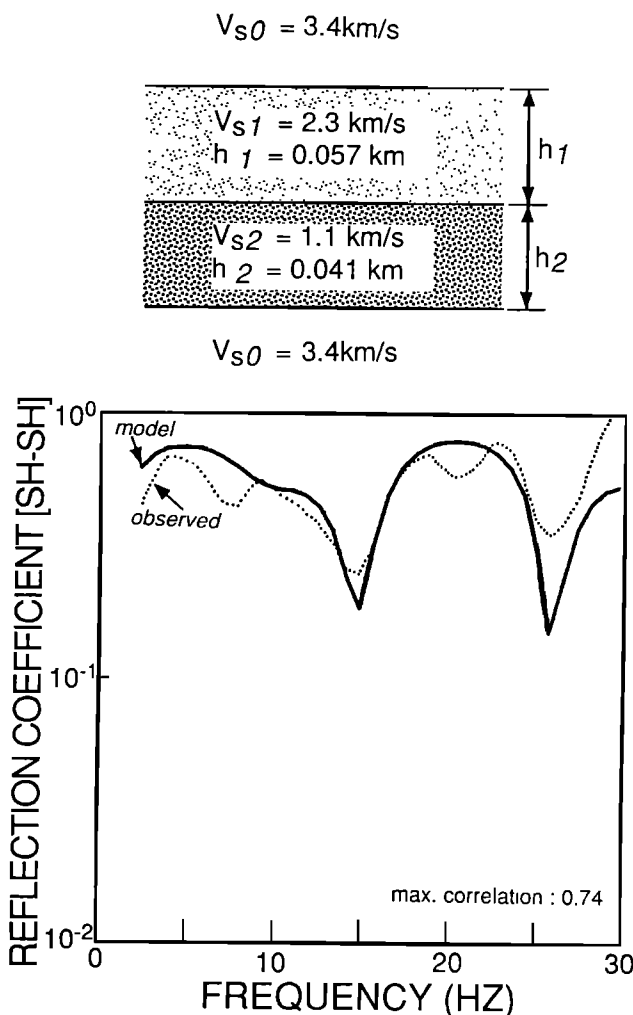
structure model

$$V_{S0} = 3.4km/s$$

$V_{S1} = 2.3 \, km/s$
$h_1 = 0.057 \, km$

h_1

$V_{S2} = 1.1 \, km/s$
$h_2 = 0.041 \, km$

h_2

$$V_{S0} = 3.4km/s$$

model

observed

REFLECTION COEFFICIENT [SH-SH]

10^0

10^{-1}

10^{-2}

max. correlation : 0.74

0   10   20   30

FREQUENCY (HZ)

Figure 16. Same as Figure 15, but for a two-layer model.

a)

max. 90% 80% max. correlation= 0.74

V_{S0} = 3.4km/s

V_{S1} =0.1 - 3.3km/s
h₁ =0.001 - 1.745km   h₁

V_{S2} = 1.1 km/s
h₂ = 0.041 km   h₂

V_{S0} = 3.4km/s

S-WAVE VELOCITY (km/s) [layer 1]

LAYER THICKNESS (km) [layer 1]

b)

max. 90% 80% max. correlation= 0.74

V_{S0} = 3.4km/s

V_{S1} =2.3km/s
h₁ =0.057 km   h₁

V_{S2} =0.1 - 3.3km/s
h₂ =0.001 - 1.745km   h₂

V_{S0} = 3.4km/s

S-WAVE VELOCITY (km/s) [layer 2]

LAYER THICKNESS (km) [layer 2]
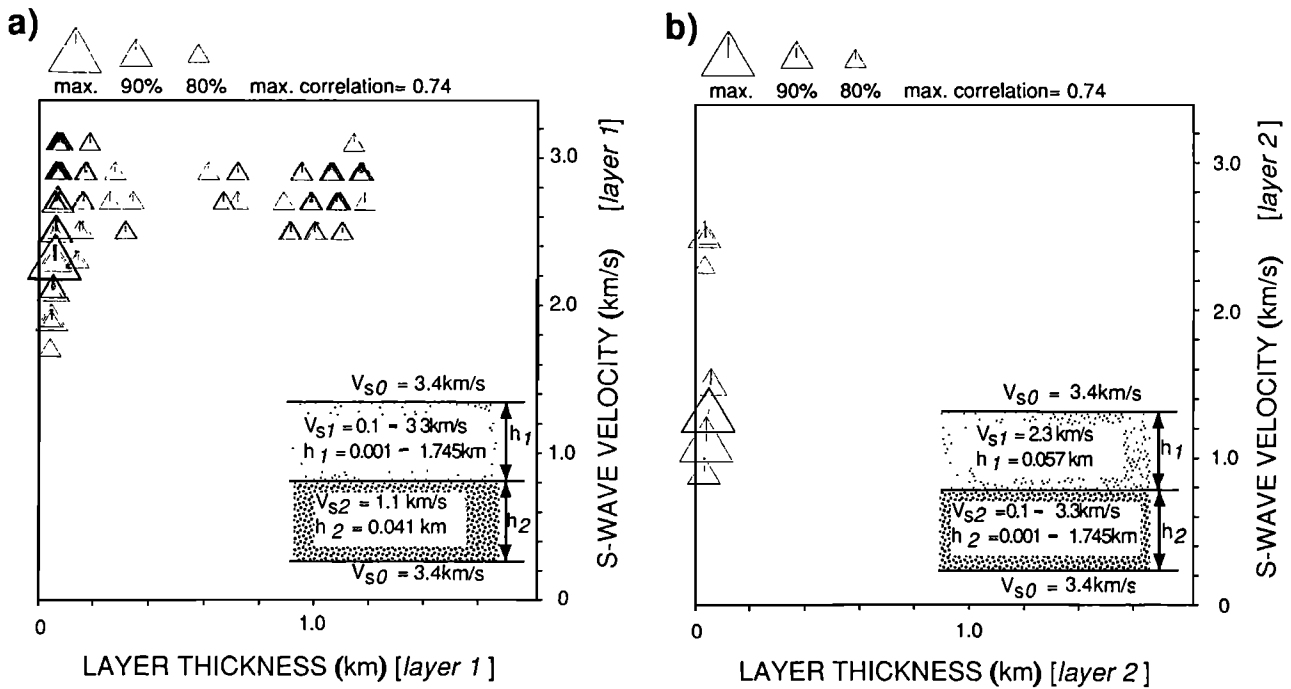
Figure 17. Distribution of correlation coefficient for a two layer model. Symbols are the same as in Figure 14. (a) Correlation coefficients are plotted on the $Vs1$-$h1$ plane for the case of $Vs2$=1.1 km/s and $h2$=0.041 km. (b) Correlation coefficients are plotted on the $Vs2$-$h2$ plane for the case of $Vs1$=2.3 km/s and $h1$=0.057 km.

stable-sliding transition zone [e.g., *Brace and Byerlee*, 1970; *Meissner and Strehlau*, 1982; *Sibson*, 1982; *Tse and Rice*, 1986]. Namely, it seems that the reflector body readjusts locally the thermal structure in its surrounding area.

Recently a deep, low-frequency microearthquake was detected just below the reflector presently located (S. Tsukada and T. Urabe, personal communication, 1994). This event has anomalously low predominant frequencies both for *P* and *S*

89 8 26 -> 89 11 17

36°30'N   36°40'N   36°50'N

KM

0

10

20

REFLECTOR

Figure 18. NS vertical cross section of earthquakes (circles) in the Nikko-Ashio area. Estimated locations of the reflection points are also shown by crosses. A triangle and crosses at the top denote the locations of Nikko-Shirane volcano and observation stations, respectively. Solid line indicates surface topography.

waves and an anomalously deep focal depth (~35 km) well below the cutoff depth of shallow seismicity, similarly to those detected at 12 other locations beneath active volcanoes and/or in or around the *P* wave low-velocity zones in northeastern Japan [*Hasegawa et al.*, 1991, 1993]. These deep low-frequency microearthquakes are anomalous events either with extremely low stress drops or with extremely low rupture velocities, and are caused perhaps by magmatic activity in the lowermost crust or the uppermost mantle [*Hasegawa et al.*, 1991, 1993]. The deep low-frequency microearthquakes are occurring right under all the *S* wave reflectors in the midcrust detected so far at five locations in northeastern Japan, including the present case. The deep structure of arc volcanism is reflected in these recent seismic observations: midcrustal *S* wave reflectors, *P* wave low-velocity zones, and deep low-frequency microearthquakes. They are closely related to a magma supplying system in the crust and mantle wedge beneath volcanic arcs, as discussed by *Hasegawa* and *Zhao* [1994].

All the observations described above suggest that the midcrustal reflector is composed of a partially molten body. However, it is known that such a thin magma body with a thickness of about 100 m easily solidifies after several tens of years have elapsed. We estimate the reflector body at present is in the following state. Nikko-Shirane volcano erupted about 40 years ago. magma certainly existed at that time even in the very shallow region beneath the volcano. The midcrustal reflector body was filled with molten materials and its original thickness was perhaps thicker than the present one. The magma body has been cooled continuously and has gradually solidified from its upper and lower edges with time. During this cooling process, the cooling rate of the body would be reduced if additional magma is supplied from the uppermost mantle, which we think
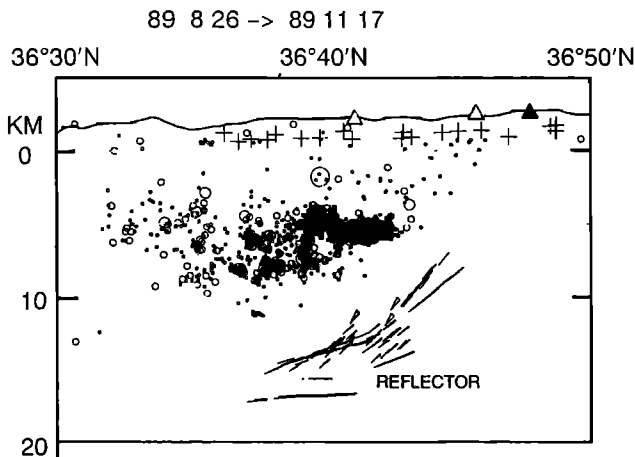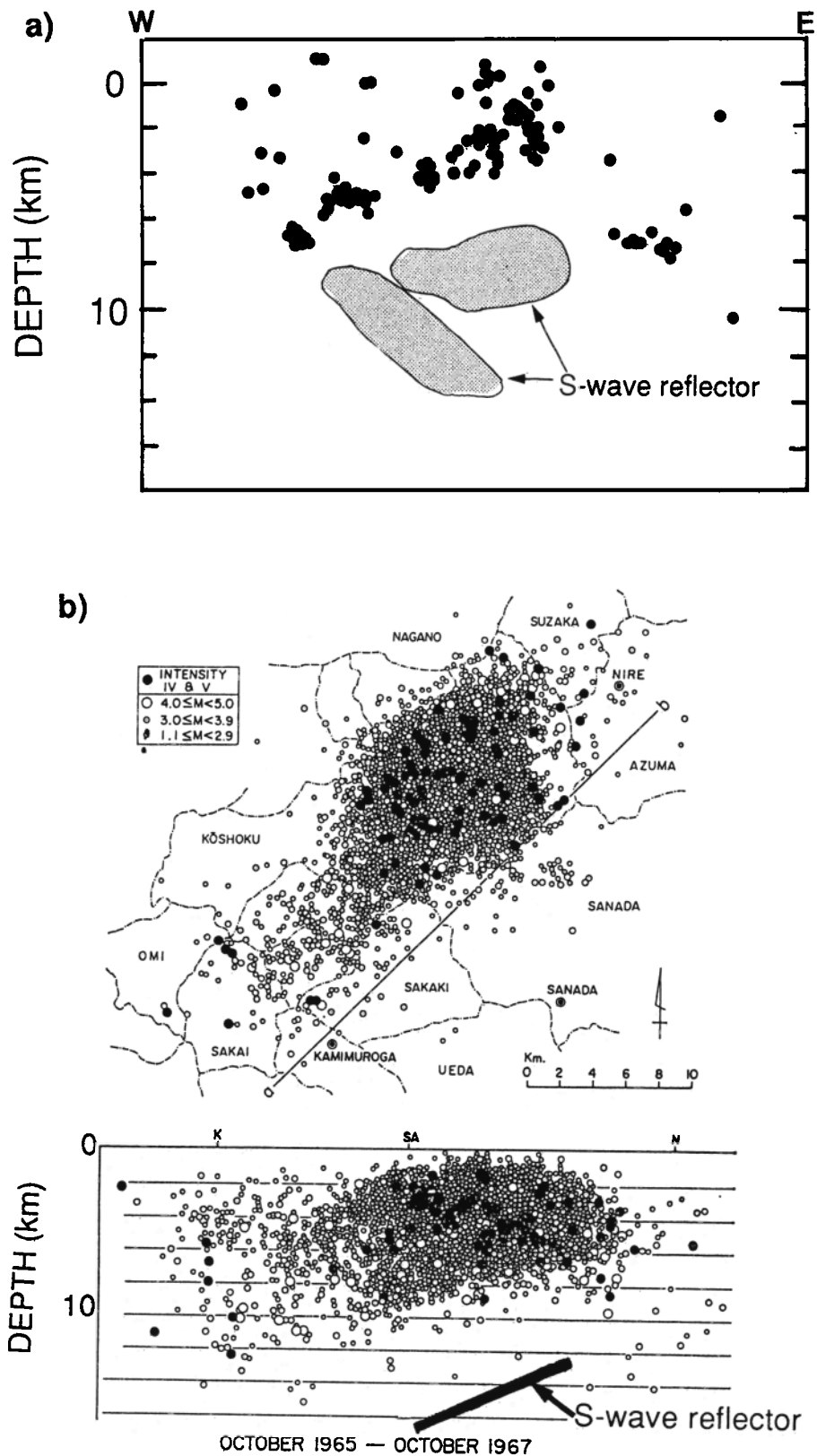
Figure 19. Geometrical relationship between the S wave midcrustal reflector and the cutoff depth for shallow seismicity. (a) EW vertical cross section of aftershocks (solid circles) of the 1984 Western Nagano Earthquake and the midcrustal S wave reflector [*Inamori et al.*, 1992]. (b) (Top) Epicenter distribution and (bottom) NE-SW vertical cross section of earthquakes in the Matsushiro earthquake swarm for the period October 1965 to October 1967 [*Hagiwara and Iwata*, 1968]. Hypocenters are shown by circles. The midcrustal S wave reflector detected by *Nishiwaki et al.* [1989] is also shown by a bold line on the vertical section.

is quite probable. At present the body is still cooling and has not yet solidified completely.

In conclusion, the results obtained in the present study are summarized as follows.

1. The midcrustal reflector which excites remarkable reflection phases has been detected beneath the Nikko-Ashio area. It spreads over an area of 15 km x 15 km at depths ranging from 8 to 15 km. It has a conical shape shallowing toward Nikko-Shirane volcano.

2. The reflector body has a total thickness of about 100 m or less. It is composed of at least two-layers with extremely low S wave velocities. The reflector body possibly contains in part a kind of liquid such as a magma or water.

3. The lower limit of shallow seismicity in this area becomes shallow toward the volcano, and the reflector is nearly parallel to the lower limit of shallow seismicity. This observation suggests that the depth to brittle-ductile transition zone is prescribed by the reflector, which is perhaps a partially molten layer.

References

Ake, J. P., and A. R. Sanford, New evidence for the existence and internal structure of a thin layer of magma at mid-crustal depths near Socorro, New Mexico, *Bull. Seismol. Soc. Am., 78*, 1335-1359, 1988.

Brace, W. F., and J. D. Byerlee, California earthquakes: Why only shallow focus?, *Science, 168*, 1573-1575, 1970.

Hagiwara, T. and T. Iwata, Summary of the seismographic observation of Matsushiro swarm earthquakes, *Bull. Earthquake Res. Inst., 46*, 485-515, 1968.

Hasegawa, A., and D. Zhao, Deep structure of island arc magmatic regions as inferred from seismic observations, in *Magmatic Systems*, edited by M. P. Ryan, pp. 167-178, Academic, San Diego, Calif., 1994.

Hasegawa, A., D. Zhao, S. Hori, A. Yamamoto, and S. Horiuchi, Deep structure of the northeastern Japan arc and its relationship to seismic and volcanic activity, *Nature, 352*, 683-689, 1991.

Hasegawa, A., A. Yamamoto, D. Zhao, S. Hori, and S. Horiuchi, Deep structure of arc volcanoes as inferred from seismic observations, *Philos. Trans. R. Soc. London. A, 342*, 167-178, 1993.

Hori, S., and A. Hasegawa, Location of a mid-crustal magma body beneath Mt. Moriyoshi, northern Akita Perfecter, as estimated from reflected SxS phases., *J. Seismol. Soc. Jpn., 44*, 39-48, 1991.

Horiuchi, S., A. Hasegawa, A. Takagi, A. Ito, M. Suzuki, and H. Kameyama, Mapping of a melting zone near Mt. Nikko-Shirane in northern Kanto, Japan, as inferred from SxP and SxS reflections, *Tohoku Geophys. J., 31*, 43-55, 1988.

Inamori, T., S. Horiuchi, and A. Hasegawa, Location of mid-crustal reflectors by a reflection method using aftershock waveform data in the focal area of the 1984 Western Nagano Prefecture Earthquake, *J. Phys. Earth, 40*, 379-393, 1992.

Ito, A., et al., Microearthquake activity in the Nikko-Ashio area, Western part of Tochigi Prefecture, Japan, *Zisin, 2*(47), 287-302, 1994.

Ito, A., M. Suzuki, Y. Haryu, A. Hasegawa S. Matsumoto, and M. Kasahara, Characteristic microearthquakes occurring beneath Mt. Nikko-Shirane that look like tremors, *Programme Abstr. Jpn. Earth Planet. Sci. Joint Meet.*, p. 276, 1995.

Iwase, R., S. Urabe, K. Katsumata, M. Moriya, I. Nakamura, and M. Mizoue, Mid-crustal magma body in southwestern Fukushima Prefecture detected by reflected waves from microearthquakes, *Programme Abstr. Seismol. Soc.* Jpn., no.1, 185, 1989.

Kennett, B. L. N., and N. J. Kerry, Seismic waves in a stratified half space, *Geophys. J. R. . Soc., 57*(3), 557-584, 1979.

Meissner, R., and J. Strehlau, Limits of stresses in continental crusts and their relation to the depth-frequency distribution of shallow earthquakes, *Tectonics, 1*, 73-89, 1982.

Mizoue, M., Deep crustal discontinuity underlain by molten material as deduced from reflection phases on microearthquake seismograms, *Bull. Earthquake Res. Inst. Univ. Tokyo, 55*, 705-735, 1980.

Mizoue, M., and Y. Ishiketa, Detection of melting zone beneath fault area of the 1984 Western Nagano Prefecture Earthquake and beneath the sourthern foot of Mt. Ontake, (in Japanese), *Gekkan Chikyu (Earth Monthly), 10*, 700-705, 1988.

Mizoue, M, I., Nakamura, and T. Yokota, Mapping of an unusual crustal discontinuity by microearthquake reflections in the earthquake swarm area near Ashio, northwestern part of Tochigi Prefecture, central Japan, *Bull. Earthquake Res. Inst. Univ. Tokyo, 57*, 653-686, 1982.

Mochizuki, E., K. Sakuma, and M., Imoto, Focal mechanisms of earthquakes in the Kanto-Tokai District (1979-1983), (in Japanese), *Zisin*, 2(38), 411-422, 1985.

Murase, T., and A. R. Mcbirney, Properties of some common igneous rocks and their melts at high temperatures, *Geol., Soc. Am. Bull., 84*, 3563-3592, 1973.

Nishiwaki, M., Y. Morita, S. Nagare, T. Kakishita, Y. Osada, and N. Nagai, Detection of S wave reflector beneath the Matsushiro array, central Japan, *Programme Abstr. Seismol. Soc. Jpn.*, no.1, 184, 1989.

Rinehart, E. J., A. R. Sanford, and R. M. Ward, Geographic extent and shape of an extensive magma body at mid-crustal depths in the Rio Grande rift near Socorro, New Mexico, in *Rio Grande Rift: Tectonics and Magmatism*, edited by R. Riecker, pp. 237-251 , Washington, D. C., 1979.

Sanford, A. R., O. Alptekin, and T. R. Toppozada, Use of reflection phases on microearthquake seismograms to map an unusual discontinuity beneath the Rio Grande Rift, *Bull. Seismol. Soc. Am., 63*, 2021-2034, 1973.

Sanford, A. R., R. P. Mott Jr., P. J. Shuleski, E. J. Rinehart, F. J. Caravella, R. M. Ward, and T. C. Wallace, Geophysical evidence for a magma body in the crust in the vicinity of Socorro, New Mexico, in *The Earth's Crust, Geophys. Monogr. vol. 20*, edited by J. G. Heacock, pp. 385-403, AGU, Washington, D. C., 1977.

Sibson, R. H., Fault zone models, heat flow, and the depth distribution of earthquakes in the continental crust of the United States. *Bull. Seismol. Soc. Am., 72*, 151-163, 1982.

Tse, S. T. and J. R. Rice, Crustal earthquake instability in relation to the depth variation of frictional slip properties, *J. Geophys. Res., 91*, 9452-9472, 1986.

Zhao, D., A. Hasegawa, and S. Horiuchi, Tomographic imaging of P and S wave velocity structure beneath northeastern Japan, *J. Geophys. Res., 97*, 19,909-19,928, 1992.

S. Matsumoto A. Hasegawa, Observation Center for Prediction of Earthquakes and Volcanic Eruptions, Faculty of Science, Tohoku University, Sendai 980-77, Japan.